*Acta Cryst.* (1998). A**54**, 102–119

# Corrections for Multiple Scattering in Integrated Electron Diffraction Intensities. Application to Determination of Structure Factors in the [001] Projection of $Al_mFe$

KJERSTI GJØNNES,[a]* YIFAN CHENG,[b] BJØRN S. BERG[a] AND VIDAR HANSEN[a]

[a]*Department of Physics, University of Oslo, PO Box 1048, 0316 Oslo 3, Norway, and* [b]*Max Planck Institut für Metallforschung, Institut für Werkstoffwissenschaft, Seestrasse 92, 70172 Stuttgart, Germany.*
*E-mail: kjersti.gjonnes@ah.telia.no*

(*Received 18 March 1997; accepted 31 July 1997*)

## Abstract

Approximate methods are described for treating dynamical scattering effects in integrated electron diffraction intensities from unknown structures. In the application to $Al_mFe$, ($hk0$) structure factors have been determined by combining data from two electron diffraction techniques: energy-filtered convergent-beam electron diffraction (CBED) profiles from the ($h00$) and ($hh0$) systematic rows and integrated intensity collected by the precession technique in the [001] projection. The *ab initio* determination of the ($h00$) and ($hh0$) structure factors was based on accurate intensity measurements and $n$-beam dynamical scattering calculations for the systematic row. The remaining ($hk0$) structure factors were determined from integrated intensities by means of two-beam-like intensity expressions and the effect of other beams was accounted for by a dynamical potential.

## 1. Introduction

Crystal structure determination from electron diffraction intensities is a rapidly growing field. Efforts towards development of standard procedures has progressed along two lines: a kinematic approach with adaption and modification of techniques from X-ray crystallography (Dorset 1994; Dorset, Kopp, Fryer & Tivol, 1995; Bricogne & Gilmore, 1990), sometimes combined with information from high-resolution images (Zou, Sundberg, Larine & Hovmöller, 1996; Weirich, Ramlau, Simon, Hovmöller & Zou, 1996), or a multiple-scattering approach where the dynamical theory is incorporated in crystallographic methods specifically designed for electron diffraction (Spence, 1993).

The effect of dynamical scattering, appreciable at large thicknesses, on electron diffraction intensities is strongly dependent on diffraction conditions. This has led to two radically different approaches to crystal structure determination by electron diffraction. One is based on energy-filtered convergent-beam electron difffraction (CBED) profiles taken in orientations with enhanced dynamical scattering, giving a high sensitivity to structure details, suitable for the determination of a few very accurate structure factors. The alternative, which is more suited to the determination of unknown structures, is to extract integrated intensities from off-axis orientations, where dynamical scattering is reduced, and approximations in terms of two or a few beams can be applied. In this paper, we show how these two approaches have been combined in the study of the unknown structure $Al_mFe$.

In the first approach, the sensitivity of electron diffraction is fully exploited by seeking orientations where dynamical effects are maximized. Energy-filtered one- or two-dimensional CBED profiles are measured and subsequently fitted to theoretical curves for determination of accurate structure-factor amplitudes or phases, usually in small unit cells (Bird & Saunders, 1992; Zuo, Spence & O'Keeffe, 1988; Gjønnes, Gjønnes, Zuo & Spence, 1988). Very accurate structure parameters can be obtained but this requires extensive calculations, even in the case of refinement of a few structure factors in otherwise known structures (Saunders *et al.*, 1995; Saunders, Bird, Midgley & Vincent, 1994). Application to unknown structures, on the other hand, would require approximations in terms of few beams, at least in the initial stages of refinement. In an *ab initio* determination of ($h00$) and ($hh0$) structure factors in $Al_mFe$ (Cheng, Nüchter, Mayer, Weickenmeier & Gjønnes, 1996; and this paper) from energy-filtered systematic row CBED intensity profiles, structure factors were determined iteratively, starting from a two-beam description of the strongest reflection in the systematic row, and gradually including more reflections in the calculations. The method can, in principle, be extended to two rows or three- and four-beam cases coupled by reflections already determined and finally to projections. This would, however, comprise a formidable task.

The use of integrated intensities in structure determination represents a different approach, more suited to the determination of unknown structures. Integrated intensities extracted from CBED patterns by integration across $K$-line segments in systematic rows (Taftø & Metzger, 1985), in higher-order Laue-zone (HOLZ) rings (Vincent, Bird & Steeds, 1984; Vincent & Bird, 1986) or in off-axis orientations are less sensitive to thickness and less affected by non-systematic many-beam dynamical

scattering. By integration over diffraction conditions, contributions from many-beam interactions are averaged and dynamical effects are thus even further reduced. The sensitivity of the diffraction data to the crystal structure details may be reduced in such experiments but the sensitivity to thickness and other experimental parameters is also reduced. Integrated intensities can be extracted from systematic rows and off-axis orientations but a more practical way to collect a full three-dimensional set of intensities is provided by the Vincent & Midgley (1994) technique, where the tilted beam is precessed about the zone axis. Below the objective lens, the beam is descanned to produce a diffraction pattern, where each spot corresponds to the integrated intensity of one reflection. Thus, all the reflections in a projection can be measured in a single exposure and a three-dimensional set of intensities can be constructed by merging intensity data from several projections.

In this paper, we show how the two approaches described above can be combined in the study of an unknown structure, our example being the intermetallic phase $Al_mFe$ with $m \simeq 4.4$ [with space group $I\bar{4}2m$ and a tetragonal unit cell of $a = 8.84$, $c = 21.6$ Å (Gjønnes, Hansen, Berg, Midgley & Cheng, 1995)]. Structure factors in the two systematic rows ($h$00) and ($hh$0) have been determined from energy-filtered CBED intensity profiles in off-axis orientations where non-systematic effects are reduced, extending the results previously reported for the ($h$00) rows (Cheng, Nüchter, Mayer, Weickenmeier & Gjønnes, 1996). The remaining structure factors in the [001] projection have been determined from integrated intensities obtained by the Vincent–Midgley technique using a two-beam approach, where the effect of other beams is included through an effective potential. The complete three-dimensional intensities obtained by the precession technique are currently being used in a structure determination of $Al_mFe$ based on a kinematic interpretation of the intensities (Gjønnes *et al.*, 1998) by employing a number of crystallographic methods adapted from X-ray diffraction. Treating intensities as kinematic obviously simplifies the structure determination but at the risk of losing information distorted by strong dynamical diffraction effects. The purpose of the present paper is to demonstrate that structure factors in a projection can be determined from a combination of energy-filtered CBED profiles in systematic rows and integrated intensities at a much poorer accuracy and to show that this procedure does indeed bring out new structure information compared with a purely kinematic interpretation of the intensities.

## 2. Determination of ($hh$0) structure factors from energy-filtered CBED profiles

The first step towards the goal defined in the *Introduction* is to determine the structure factors in the unknown structure $Al_mFe$ from systematic row CBED patterns. The extension of this method to unknown structures was published by Cheng, Nüchter, Mayer, Weickenmeier & Gjønnes (1996) for the ($h$00) row in $Al_mFe$. Those results are reproduced here, but for a more detailed description of the refinement procedure see Cheng *et al.* (1996). The present treatment has been extended to include the ($hh$0) row.

Table 1. *Structure factors and Bethe potentials in the ($h$00) systematic row*

| | | Bethe potential | |
|---|---|---|---|
| $hkl$ | Structure factor $U_g$ in Å$^{-2}$ | Sytematic only ($h$00) | Non-systematic ($h$00) and ($hh$0) |
| 200 | −0.01191 (31) | −0.01461 | −0.01456 |
| 400 | 0.01592 (44) | 0.01079 | 0.01066 |
| 600 | 0.01275 (16) | 0.01742 | 0.01729 |
| 800 | −0.00653 (72) | −0.00624 | −0.00616 |
| 10,0,0 | 0.00359 (33) | 0.00152 | −0.00147 |
| 12,0,0 | −0.00135 (18) | −0.00072 | −0.0071 |
| 14,0,0 | −0.00214 (31) | −0.00220 | −0.00225 |

Table 2. *Structure factors and Bethe potentials in the ($hh$0) systematic row*

| | | Bethe potential | |
|---|---|---|---|
| $hkl$ | Structure factor $U_g$ in Å$^{-2}$ | Sytematic only ($hh$0) | Non-systematic ($h$00) and ($hh$0) |
| 110 | 0.0029 (45) | 0.00387 | 0.00517 |
| 220 | −0.00199 (23) | 0.00214 | 0.00308 |
| 330 | 0.0387 (9) | 0.03976 | 0.03980 |
| 440 | 0.00750 (34) | 0.00523 | 0.00399 |
| 550 | 0.00773 (107) | 0.00910 | 0.00891 |
| 660 | 0.00226 (51) | −0.00407 | −0.00428 |
| 770 | 0.00158 (27) | 0.00001 | 0.00000 |
| 880 | 0.00514 (40) | 0.00368 | 0.00400 |
| 990 | 0.00300 (18) | 0.00228 | 0.00219 |
| 10,10,0 | 0.00140 (11) | 0.00104 | 0.00076 |
| 11,11,0 | 0.00210 (8) | 0.00137 | 0.00455 |

Energy-filtered CBED patterns from the ($h$00) and ($hh$0) systematic rows were taken at 120 kV using a Zeiss EM912 equipped with an omega filter. CBED patterns acquired with a slow-scan CCD camera were deconvoluted with the point-spread function of the CCD camera and introduced into the structure-factor-determination scheme. The CBED patterns were taken near the Bragg condition for reflections in the two systematic rows ($h$00) and ($hh$0). Interferences from non-systematic reflections were minimized by careful tilting into orientations where few non-systematic reflections were excited. Several diffraction patterns, at different thicknesses and orientations, were recorded for each of the two rows. The structure factors listed in Tables 1and 2 are the averages of structure-factor determinations based on all of these.

The refinement procedure utilized programs originally developed by Zuo & Spence (1991) and modified by Nüchter, Weickenmeier & Mayer (1995). Only systematic reflections were included and absorption was ignored. Structure factors as well as thickness, diffraction

condition and orientation of the reciprocal vector relative to the camera were refined. An iterative approach was used for the structure-factor refinement. The structure-factor amplitude and thickness were determined for the strongest reflection in the systematic row, *i.e.* 600 in the (*h*00) row and 330 in the (*hh*0) row, using a two-beam approximation. Then low-order structure factors were refined using four beams: 200, 400 and 600 in the (*h*00) row and 110, 220 and 330 in the (*hh*0) row. Signs were determined by using a range for the structure factors including both negative and positive values. The refinement of the structure factors for the strongest reflections, 600 and 330, was then improved using four beams in the calculations. Higher-order reflections were gradually introduced into the calculations and refined while keeping the low-order structure factors constant. After approximations had been derived for all the structure factors, the refinement of the low-order reflections was repeated using all 15 and 23 beams for the (*h*00) and (*hh*0) rows, respectively. See Fig. 1 for a comparison between calulated and experimental intensity profiles in the (*hh*0) row. At intermediate stages in the refinement described above, multiple solutions with comparable $\chi^2$ could be found but we were able to distinguish between these in the further refinement. The resulting structure factors are listed in Tables 1 and 2.

The signs within the (*h*00) and (*hh*0) rows in Tables 1 and 2 are relative signs referring to an isolated row. The symmetry in the [001] projection is 4*mm* (Gjønnes *et al.*, 1995), where (*hk*0) and ($h\bar{k}$0) have the same sign. The signs of 4*n*,0,0 and 2*n*,2*n*,0 reflections are invariant under a change of origin. When the sign has been chosen for one of the remaining (*h*00) and (*hh*0) reflections, the origin is defined. The rest of the signs will then be determined by the choice of the origin. A further discussion of the signs is defered to §3.4.

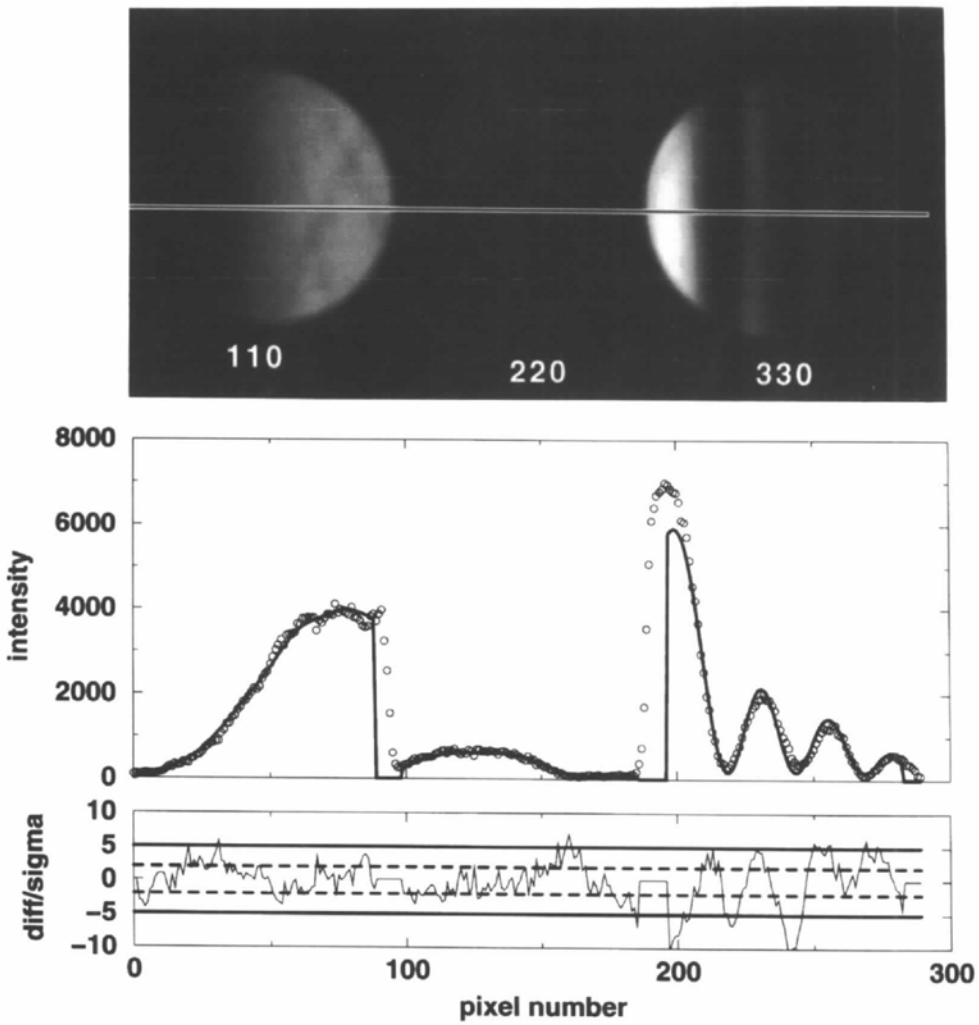


Fig. 1. Refinement of (*hh*0) structure factors from systematic row CBED intensity profiles.

## 3. Determination of structure factors in the [001] projection from integrated intensities

In the previous section, we have described the determination of ($h00$) and ($hh0$) structure factors from CBED intensity profiles. In this section, we present procedures aimed at extracting corrected near-kinematic intensities from experimental integrated intensities obtained with the Vincent–Midgley precession technique. The application to the [001] projection of $Al_mFe$ is discussed in detail in the following and only a brief outline is given here.

An approximate description of the dynamical scattering in terms of a perturbed two-beam case forms the basis for the procedure for extraction of structure factors from the precession data. The effects of other beams are included through an effective (dynamical) potential given by Bethe (1928):

$$U_g^{\text{Bethe}} = U_g - \sum_{h \neq g} (U_h U_{g-h}) / 2ks_h,$$

which can be substituted for the structure factor in expressions for the integrated intensity as a function of thickness. This is justified, since the precession technique uses off-axis orientations where relatively few beams are simultaneously excited and these are only weakly coupled.

Several steps are needed to obtain structure factors from the precession data, some of these make extensive use of the subset of structure factors determined earlier (see §2). The first step is to correct the experimental precession intensities by correcting for the geometrical factors introduced by the precession technique and obtain $\int I_g \, ds_g$ for comparison with the kinematic expression or approximations in terms of two beams. The relative integrated intensities, and possibly also the dynamical potentials, depend on the crystal thickness and the first step is therefore to determine the thickness for the precession data. The relative intensities in the two systematic rows ($h00$) and ($hh0$), where the structure factors were known from CBED measurements, were used for determination of the thickness for the precession data. Corrections for two-beam dynamical effects could then be calculated at this thickness using the two-beam expression for the integrated intensity (Blackman, 1939):

$$\int_{-\infty}^{\infty} I_g(s_g) \, ds_g \propto A_g \int_0^{A_g} J_0(x) \, dx$$

with $A_g = 2\pi U_g z/k$, the result being effective potentials in the [001] projection. The final step in the procedure is to calculate the structure factors (including signs) from the effective potential amplitudes using the Bethe equations. Signs are therefore needed for the effective potentials, which were determined using symbolic addition methods utilizing the relative signs within the ($h00$) and ($hh0$) rows and positive triplets including the ($hk0$) reflections. When the signs had been determined, the structure factors could be calculated by an iterative reversal of the Bethe equation for the dynamical potentials. Finally, as a check of the procedure, $n$-beam dynamical calculations of integrated intensities starting from the ($hk0$) structure factors determined here were compared with the experimental intensities.

### 3.1. *Measurement of integrated intensities in the [001] projection*

Integrated ($hk0$) intensities were extracted from electron diffraction negatives taken with the precession technique (Vincent & Midgley, 1994) by integration of the intensity within each reflection (spot) (Berg, 1996; Berg, Hansen, Midgley & Gjønnes, 1997). The measured intensities (see Table 3) thus result from a double integration, first over the rotation angle in the plane, $\theta$ in Fig. 2, during the precession of the beam and then over

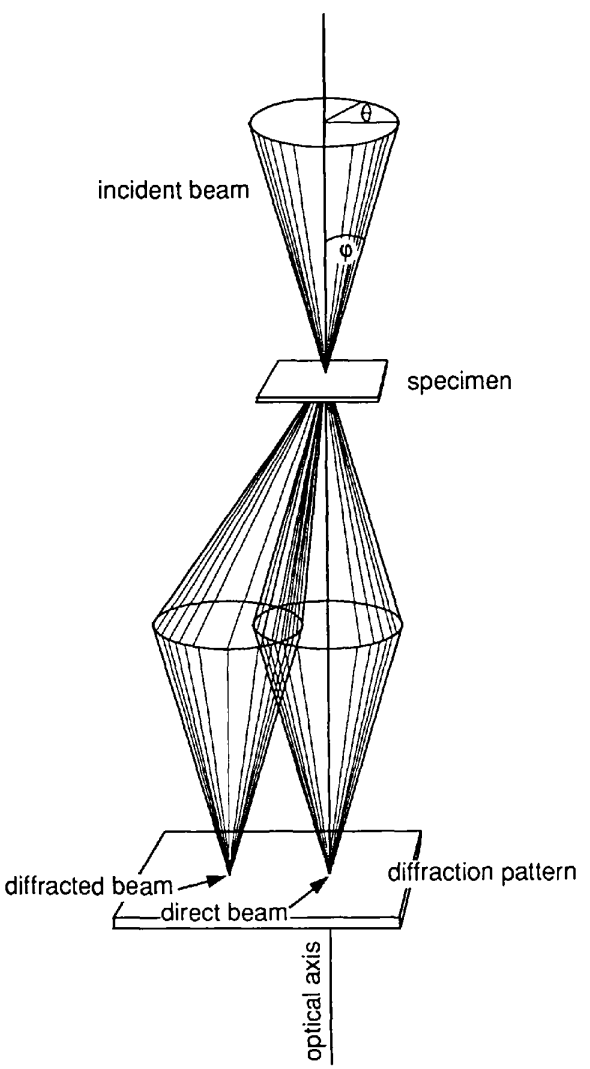


Fig. 2. The precession geometry.

$k_{xy}$, the projection of **k** onto the ($hk0$) plane during the recording of the intensity from the negative. Intensities therefore needed to be corrected for the geometrical factors associated with the precession. Correction factors, similar to the Lorentz factors used in X-ray diffraction, have previously been derived by Gjønnes (1997*a*) and are reproduced here for the zero-order Laue zone.

Let us first consider the integration over $\theta$ when there is no beam divergence:

$$I_g^{\rm exp} \propto \int_0^{2\pi} I_g(\theta)\,{\rm d}\theta \qquad (1)$$

with $\theta$ the angle in Fig. 2 and $I_g$ the intensity in reflection $g$. For comparison with two-beam or kinematical approximations, we need the integral over the excitation error $s_g$, *i.e.*

$$\int_{-\infty}^{\infty} I_g(s_g)\,{\rm d}s_g. \qquad (2)$$

In the zero-order Laue zone, the integration over $\theta$ in (1) can be transformed to an integration over the excitation error $s_g$ by observing that (see Fig. 3)

$$2ks_g = -2k_g g - g^2 = -2Rg\cos\theta - g^2 \qquad (3)$$

and hence

$$2k\,{\rm d}s_g = Rg\sin\theta\,{\rm d}\theta, \qquad (4)$$

where $R$ is the radius of the Laue circle. The intensity in $g$, $I_g(\theta)$, is significant only in a small region near the Bragg condition for $g$, allowing us to write $\sin\theta = [1-(g/2R)^2]^{1/2}$ outside the integral and

$$\int_0^{2\pi} I_g(\theta)\,{\rm d}\theta = 2\{1/Rg[1-(g/2R)^2]^{1/2}\}\int_{-\infty}^{\infty} I_g(s_g)\,{\rm d}s_g, \qquad (5)$$

where the factor 2 takes care of the fact that the Bragg condition is encountered twice in each precession cycle. The derivation can easily be extended to include higher-order Laue zones (Gjønnes, 1997*a*). Equation (5) differs

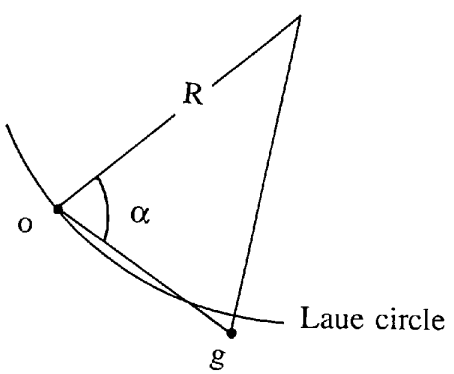


Fig. 3. The excitation error in the precession geometry.

Table 3. *Integrated intensities in the [001] projection*

| $hkl$ | $d$ | Experimental integrated intensities $I_g^{\rm exp}$ | Corrected intensities $I_g^{\rm exp}[1-(g/2R)^2]$ |
|---|---|---|---|
| 110 | 6.25 | 100.94 | 100.75 |
| 200 | 4.42 | 312.56 | 311.39 |
| 220 | 3.13 | 171.07 | 169.80 |
| 310 | 2.80 | 170.15 | 168.57 |
| 330 | 2.08 | 629.98 | 619.36 |
| 400 | 2.21 | 289.78 | 285.45 |
| 420 | 1.98 | 25.48 | 25.01 |
| 440 | 1.56 | 70.94 | 68.81 |
| 510 | 1.73 | 16.65 | 16.24 |
| 530 | 1.52 | 279.02 | 270.22 |
| 550 | 1.25 | 313.13 | 298.52 |
| 600 | 1.47 | 441.30 | 426.41 |
| 620 | 1.40 | 9.09 | 8.75 |
| 640 | 1.23 | 5.45 | 5.19 |
| 660 | 1.04 | 174.74 | 162.96 |
| 710 | 1.25 | 94.74 | 90.32 |
| 730 | 1.16 | 36.02 | 34.07 |
| 750 | 1.03 | 5.32 | 4.95 |
| 770 | 0.89 | 11.41 | 10.36 |
| 800 | 1.11 | 197.59 | 185.90 |
| 820 | 1.07 | 160.04 | 149.85 |
| 840 | 0.99 | 1.04 | 0.96 |
| 860 | 0.88 | 123.34 | 111.73 |
| 910 | 0.98 | 1.90 | 1.76 |
| 930 | 0.93 | 41.70 | 38.19 |
| 950 | 0.86 | 2.41 | 2.17 |
| 970 | 0.78 | 1.18 | 1.04 |
| 10,0,0 | 0.88 | 12.19 | 11.04 |
| 10,2,0 | 0.87 | 13.67 | 12.35 |
| 10,4,0 | 0.82 | 3.58 | 3.19 |

(by a factor $g$) from the correction factor previously published by Vincent & Midgley (1994). When beam divergence is included (see below), the factor $g$ in (5) will be cancelled by other terms.

The width of the reflections (spots) in the diffraction pattern results from the small spread of directions within the incident electron beam limited by a small aperture. In a normal CBED pattern, this will produce circular discs of the same size for all the reflections in the CBED pattern. In the precession technique, with a tilted beam, the effect on low- and high-index reflections will be different. The effect of integration over the beam divergence, corresponding to an integration of intensity within the spot on the electron diffraction negative, is to multiply the intensity in (5) with additional correction factors. The detailed derivation is published elsewhere (Gjønnes, 1997*a*) but the result for the zero-order Laue zone,

$$g/\{2R[1-(g/2R)^2]^{1/2}\}, \qquad (6)$$

is valid to first order in $r/R$, with the Laue-circle radius in the zero-order Laue zone $R-r < R_{\rm Laue} < R+r$ and $r \ll R$. Combining (5) and (6) gives

$$\int_{-\infty}^{\infty} I_g(s_g)\,{\rm d}s_g \propto [1-(g/2R)^2]I_g^{\rm exp}. \qquad (7)$$

Intensities corrected for the geometrical factors in the precession according to (7) are listed in column 2 of Table 3.

### 3.2. *Determination of thickness for the precession data from reflections in the (h00) and (hh0) systematic rows*

Dynamical scattering contributions to diffraction intensities, in this case the relative intensities extracted from the precession data, depend strongly on crystal thickness. As a first step towards correcting the intensities for dynamical scattering, we therefore need to determine the crystal thickness. The precession experiment itself gives no indication of the thickness, the integrated intensity, unlike a CBED profile, contains no features suitable for refinement of the thickness for an unknown structure. However, accurate structure factors for reflections in the (*h*00) and (*hh*0) systematic rows, including relative signs within each row, have been determined from energy-filtered CBED profiles (see §2). The relative intensities within these two rows can be calculated and compared with experimental intensities for determination of thickness.

Assuming that the effect of many-beam dynamical effects can be described by effective potentials, derived in some way from the other beams in the projection, the intensity is given by a two-beam expression (Blackman, 1939):

$$I_g^{\rm exp} \propto \{U_g^{\rm eff}/[1-(g/2R)^2]\} \int_0^{A_g} J_0(x)\,{\rm d}x \qquad (8)$$

with the effective potential, $U_g^{\rm eff}$, substituted for the structure factor, $U_g$, $J_0(x)$ the Bessel function of zeroth order, $A_g = 2\pi U_g^{\rm eff} z/k$ and $k = 1/\lambda$. The integral over $J_0$ in (8) is proportional to $A_g$ for small values of $A_g$, *i.e.* for small thicknesses or weak reflections. At larger thicknesses, the kinematic approximation no longer applies and the integrated intensity oscillates with thickness until the asymptotic value proportional to $U_g^{\rm eff} z$ is reached at large thicknesses.

Preliminary calculations were carried out to investigate the dynamical scattering effects in the (*h*00) and (*hh*0) systematic rows where structure factors were known and where the relative integrated intensities could be calculated using the Blackman formula. The Bethe (1928) potentials

$$U_g^{\rm Bethe} = U_g - \sum_{h\neq g}(U_h U_{g-h})/2ks_h, \qquad (9)$$

with $2ks_h$ the excitation error of reflection $h$ at the Bragg condition for $g$, were calculated for each of the systematic rows as well as for the full set of (*h*00), (0*h*0), (*hh*0) and ($h\bar{h}$0) reflections (see Tables 1 and 2). As expected, non-systematic contributions were found to be small in the (*h*00) row and somewhat larger in the (*hh*0) row, especially in 110 and 220. While the reflections in the (*h*00) row are all strong, reflections in the (*hh*0) row range from the very strong 330 to the very weak 220, giving much stronger dynamical interactions within the row, as well as possible non-systematic dynamical effects, *e.g.* in the weak 220 from the strong 200 or involving 530 and 860 coupled by 330. The (*h*00) row was therefore considered more suited for determination of the thickness.

Integrated intensities calculated from the Blackman expression (9) were compared with experimental intensities in the (*h*00) row. A measure of the goodness of fit was defined in terms of relative integrated intensities:

$$\chi^2(z) = \sum_{g\neq h}\left[\frac{(I_g/I_h)^{\rm exp} - [I_g(z)/I_h(z)]^{\rm cal}}{(I_g/I_h)^{\rm exp} + [I_g(z)/I_h(z)]^{\rm cal}}\right]^2, \qquad (10)$$

where $z$ is the thickness, $(I_g/I_h)^{\rm exp}$ are the experimental relative intensities and $I_g(z)$ and $I_h(z)$ are integrated intensities calculated from (8). $\chi^2(z)$ was calculated from (10) for the (*h*00) systematic row using structure factors determined from CBED profiles (see §2), as well as systematic row Bethe potentials calculated from the structure factors (Tables 1–2). In both cases, a minimum is observed, though more clearly for $\chi^2(z)$ calculated from Bethe potentials (Fig. 4). The Bethe potentials represent the asymptotic value for the contributions from many-beam dynamical scattering at large thicknesses and tend to overestimate the dynamical effects at smaller thicknesses. Thickness-dependent dynamical potentials (Gjønnes, 1962)

$$U_g^{\rm dynamical}(z) = U_g - \sum_{h\neq g} T_{g,h}(z) U_h U_{g-h} \qquad (11)$$

$$T_{g,h}(z) = (1/2ks_h)\{1 - (\cos\varphi/zs_h) \times [1 - \exp(izs_h/\cos\varphi)]\}, \qquad (12)$$

with $\varphi$ the precession angle, were therefore calculated and introduced in (8) and subsequently in (10), giving the same thickness, but with no improvement in $\chi^2(z)$. This

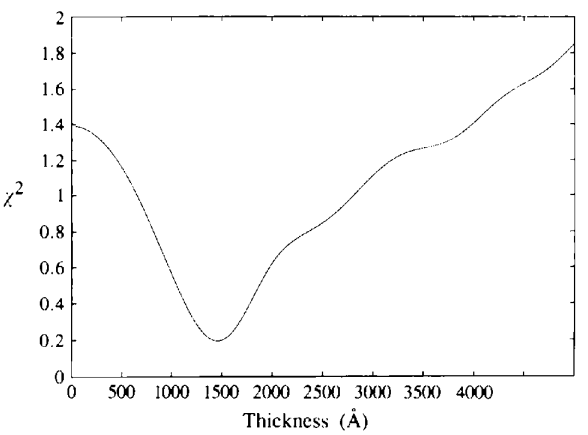


Fig. 4. Determination of thickness, fit between experimental and calculated relative intensities in the (*h*00) row as a function of thickness.

Table 4. *Integrated intensities in the [001] projection*

$n$ is the number of reflections, $n' = \sum_{i=1}^{n-1}$ is the number of relative intensities.

| Reflections | Effective potentials | Thickness (in Å) at minimum $\chi^2$ | $\chi^2/n$ | $\chi^2/n'$ |
|---|---|---|---|---|
| | Structure factors | 1000 | 0.35 | 0.175 |
| (h00) systematic row | Bethe potentials | 1500 | 0.04 | 0.02 |
| 5 reflections | Dynamical potentials | 1500 | 0.1 | 0.05 |
| | Structure factors | – | >0.8 | >0.4 |
| (*hh*0) systematic row | Bethe potentials | – | >1 | >0.5 |
| 7 reflections | Non-systematic Bethe | – | – | – |
| | Dynamical potentials | – | – | – |
| | Structure factors | – | >1.5 | – |
| (h00) + (*hh*0) | Bethe potentials | 1700 | 1.25 | – |
| 12 reflections | Dynamical potentials | 1400 | 1.5 | – |
| 200-400-600-800-330 | Structure factors | 1800 | 0.022 | 0.011 |
| | Bethe potentials | 1500 and 2600 | 0.82 | 0.41 |
| 200-400-600-800-330-550 | Structure factors | 1500 | 0.028 | 0.011 |
| | Bethe potentials | 1700 | 0.05 | 0.02 |
| 200-400-600-800-330-550-660 | Structure factors | – | >0.3 | – |
| | Bethe potential | – | >0.1 | – |

result may be taken as an indication that the thickness is large enough for the Bethe approximation (9) to the dynamical potentials to be valid.

Calculations were repeated for the (*hh*0) row, but no clear minimum in $\chi^2(z)$ was seen, either for the structure factors or the Bethe potentials. Finally, calculations were carried out including all the reflections in the (*h*00) and (*hh*0) rows, as well as for a subset of strong reflections extracted from both rows (see Table 4). The best fit to the experimental relative intensities is obtained by including only (*h*00) reflections in the refinement, giving a specimen thickness of 1500 Å.

### 3.3. *Correction for two-beam dynamical scattering*

In the previous section, we saw how the crystal thickness could be determined from the relative intensities among a small set of reflections with known structure factors. In a similar way, still using the two-beam approximation [equation (8)], we can calculate the amplitude of the effective (dynamical) potentials, $U_g$, for the rest of the reflections in the projection, with the scaling of the effective potentials provided by the thickness and at least one (effective) structure factor for a strong reflection.

In the effective two-beam approximation, where the effect of other beams is included through a dynamical potential substituted for the structure factor in the two-beam expression, relative intensities are proportional to ratios between integrals of the Bessel function. The effective potential $U_g^{\text{eff}}$ is given by

$$A_g \int_0^{A_g} J_0(x)\,\mathrm{d}x = \left(\frac{I_g}{I_h}\right)\frac{[R^2-(g/2)^2]^{1/2}}{[R^2-(h/2)^2]^{1/2}} \times A_h \int_0^{A_h} J_0(x)\,\mathrm{d}x \qquad (13)$$

with $A_g = 2zU_g^{\text{eff}}/k$, $A_h = 2zU_h^{\text{eff}}/k$, $I_g$ and $I_h$ experimental intensities, and the square root terms are derived from the Lorentz correction (see §3.1). Reflection $h$ provides the scaling of the intensities; in our case, 600, the strongest reflection in the (*h*00) row, was used.

The integral of the Bessel function in (8) and (13) exhibits damped oscillations with thickness, periodic with the extinction distance. For the strong reflections, *e.g.* 330 and 600, the extinction distances are of the order of a few hundred Å, considerably less than the actual thickness (1500 Å) at which the precession data were acquired. Experimental intensities, however, represent an average over thicknesses and diffraction conditions within the 0.5–1 μm area of the sample illuminated during precession. Thickness variations within the illuminated area comparable to the extinction distance for the strong reflections can thus be expected. This will reduce the oscillations significantly.

Integrated intensity averaged over the crystal thickness is reproduced in Fig. 5 for a few reflections in the (*h*00) and (*hh*0) rows. For reasonable thicknesses, oscillations are small and the error introduced by approximating the integrated Bessel function in (13) by a single-valued function with the same main characteristics is small compared with the uncertainties in the experimental data. An approximation, $[(\sin ax)/ax]^2$, was therefore substituted for the Bessel function in (13) in order to get a single-valued expression for $I_g(U_g z)$. The period, $a$, was chosen for the first minimum to coincide with the first minimum of the Bessel function and an exponential damping, $b$, to get the correct asymptotic behaviour at large thicknesses, giving

$$[(\sin ax)/ax]^2 \exp[-(x/b)]^2 \qquad (14)$$

with $a = \pi/2.405$ and $b = 2.565$. A comparison between (14) and the Bessel function is shown in Fig. 6.

Expression (14) was substituted for $J_0(x)$ in the further calculation. Effective potentials were then calculated by solving (13) numerically for $A_g$ in the interval $0 < A_g < A_{600}$, using the bisection method (Press, Flannery, Teukolsky & Vetterling, 1988). For ($h$00) reflections, calculated effective potentials were within 10–20% of both the structure factors and the Bethe potentials. In the ($hh$0) row, the agreement is poorer, as expected, especially for 220, 330 and 660. 220 and 660 are weak and strongly coupled to strong reflections in both the ($h$00) and ($hh$0) rows. The sensitivity to the structure factor, or rather $U_g z$, is much smaller for large thicknesses and strong reflections (see Fig. 5) and this may explain the poor accuracy in the strong 330 reflection, which is also strongly coupled to other reflections, in particular the strong 530 and 860 reflections. The effective potentials and corresponding 'two-beam corrected' intensities, $|U_g^{\text{eff}}|^2$, scaled to the experimental intensities (Table 3) are listed in Table 5. These represent an improvement of the intensity set, but further corrections are needed to remove contributions to the effective potentials from $n$-beam dynamical scattering. This is the subject of the following sections.

### 3.4. *Assigning signs to the effective potentials*

The effective structure factors determined in the previous section include contributions from many-beam dynamical scattering. The next step, to determine structure factors (amplitudes and signs) from the effective potentials, can only be performed once the signs of effective potentials are known. In this section, we will show how signs can be assigned to the effective potentials, using phase statistics based on triplets.

In a known crystal, structure effective (dynamical) potentials may be calculated from the structure factors using (9) or (11) and (12). Phase angles or, in the case of centrosymmetric crystals, signs can be assigned to the effective potentials. These will generally not be the same as the signs of the structure factors but arise through the relative signs of the different many-beam contributions to the effective potentials. It is possible that weak reflections that are strongly coupled to strong reflections will have structure factors and effective potentials of opposite sign.

The scaled potential $U(r) = \sum_g U_g \exp(2\pi i g r)$, like the electron density in X-ray crystallography, is, at least as a first-order approximation, composed of contributions

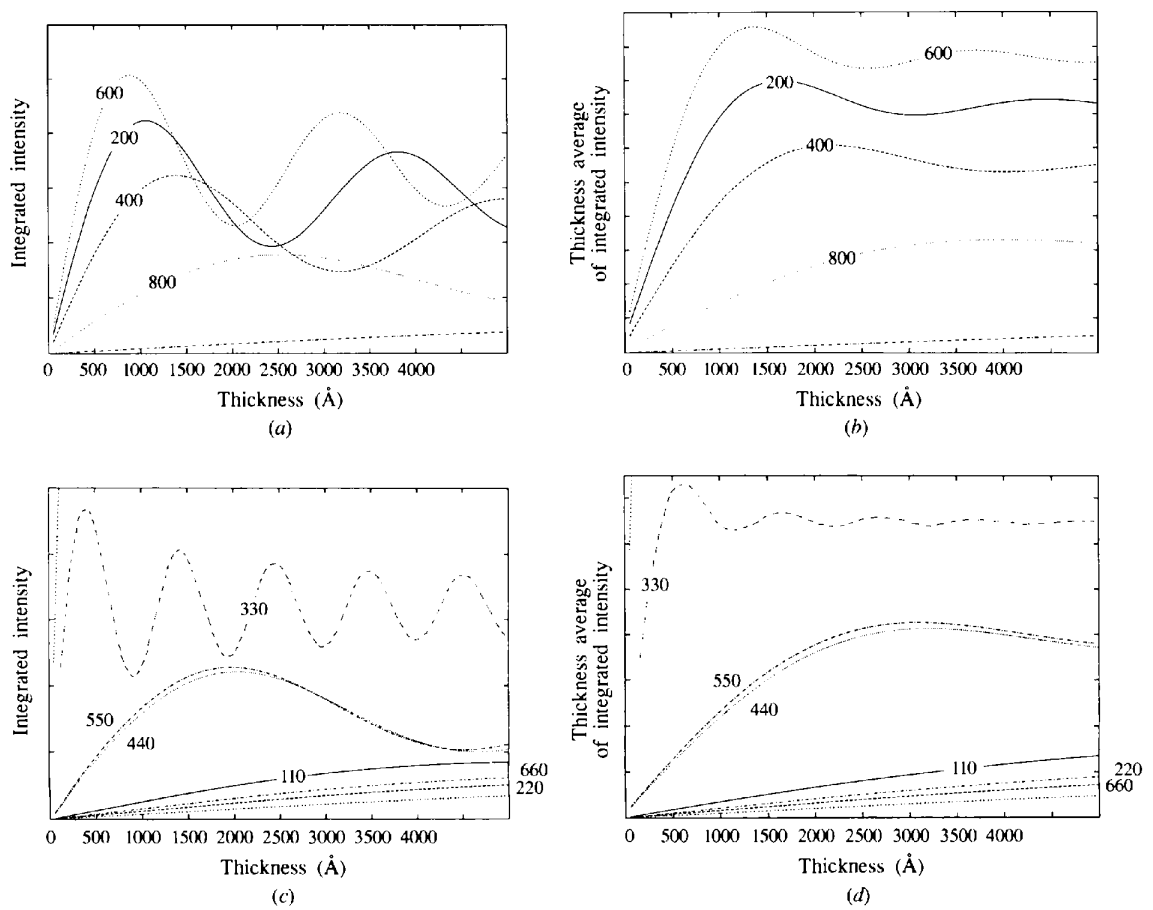


Fig. 5. Integrated intensities in (*a*) ($h$00) and (*b*) ($hh$0) rows as a function of thickness and the thickness average of the integrated intensity in (*c*) the ($h$00) row and (*d*) the ($hh$0) row.

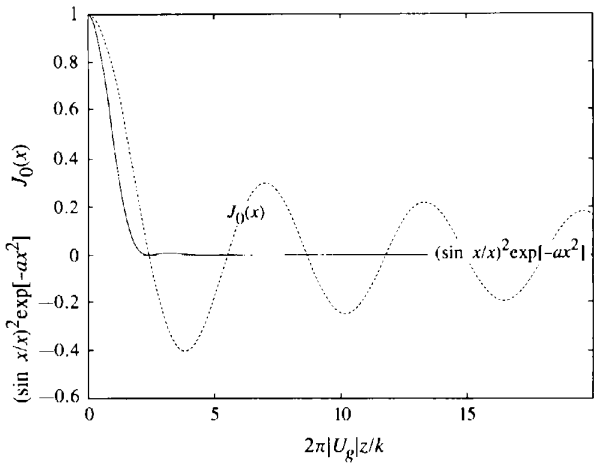


(a)

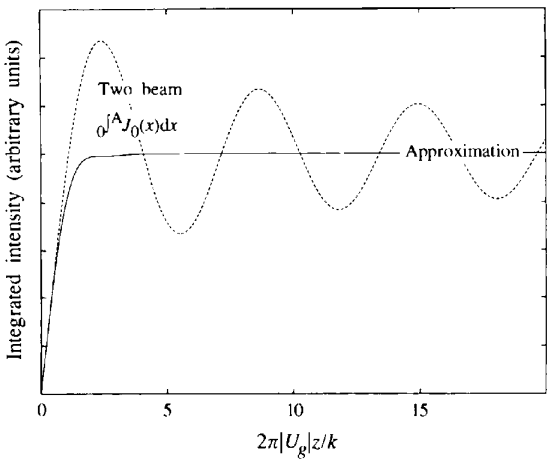


(b)

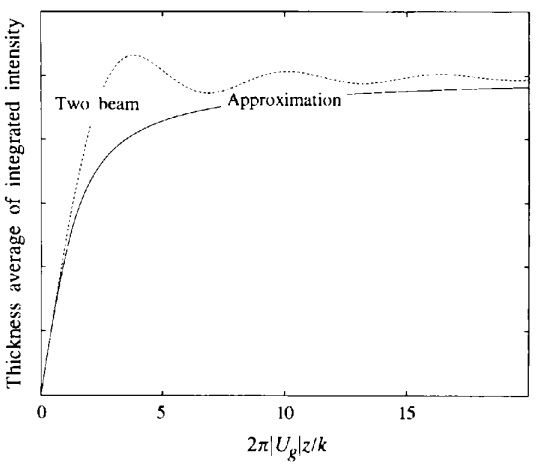


(c)

Fig. 6. (*a*) The Bessel function $J_0(x)$ and the approximation $(\sin ax/ax)^2\exp(-bx^2)$. (*b*) The two-beam integrated intensity compared with the integral over the approximation. (*c*) The thickness average of the integrated intensity calculated using the Bessel function and the approximation.

Table 5. *Effective potential amplitudes and quasi-kinematic intensities in the [001] projection*

| *hkl* | *d* | Bethe potential $U_g^{\text{Bethe}}$ | Effective potential $\lvert U_g^{\text{eff}}\rvert$ | Quasi-kinematic intensities $\propto \lvert U_g^{\text{eff}}\rvert^2$ |
|---|---|---|---|---|
| 110 | 6.25 | 0.00517 | 0.0048 | 35.34 |
| 200 | 4.42 | −0.01456 | 0.01242 | 280.30 |
| 220 | 3.13 | 0.00308 | 0.00701 | 12.54 |
| 310 | 2.80 | | 0.00697 | 64.23 |
| 330 | 2.08 | 0.03980 | | 2094.42 |
| 400 | 2.21 | 0.01066 | 0.01146 | 150.25 |
| 420 | 1.98 | | 0.00218 | 6.28 |
| 440 | 1.56 | 0.00399 | 0.00383 | 21.05 |
| 510 | 1.73 | | 0.00174 | 4.003 |
| 530 | 1.52 | | 0.01097 | 513.13 |
| 550 | 1.25 | 0.00891 | 0.01224 | 104.97 |
| 600 | 1.47 | 0.01729 | 0.01729 | 395.27 |
| 620 | 1.40 | | 0.00127 | 2.13 |
| 640 | 1.23 | | 0.00098 | 1.27 |
| 660 | 1.04 | −0.00428 | 0.00700 | 24.22 |
| 710 | 1.25 | | 0.00456 | 27.49 |
| 730 | 1.16 | | 0.00260 | 8.94 |
| 750 | 1.03 | | 0.00097 | 1.24 |
| 770 | 0.89 | 0.00001 | 0.00142 | 0.0 |
| 800 | 1.11 | −0.00616 | −0.00779 | 50.17 |
| 820 | 1.07 | | 0.00653 | 56.38 |
| 840 | 0.99 | | −0.00042 | 0.23 |
| 860 | 0.88 | | 0.00536 | 37.99 |
| 910 | 0.98 | | 0.00057 | 0.43 |
| 930 | 0.93 | | 0.00280 | 10.37 |
| 950 | 0.86 | | 0.00064 | 0.54 |
| 970 | 0.78 | | 0.00045 | 0.27 |
| 10,0,0 | 0.88 | 0.00147 | 0.00146 | 2.86 |
| 10,2,0 | 0.87 | | 0.00155 | 3.18 |
| 10,4,0 | 0.82 | | 0.00078 | 0.80 |

from resolved atoms. When structure-factor amplitudes are known, this restricts the relative phases between structure factors according to the Sayre equation (Sayre, 1952):

$$F_g = \Omega_g \sum_h F_h F_{g-h} \tag{15}$$

with $\Omega$ a calculable constant. When $F_g$ is large, the sum tends to be dominated by products between large $F_h$ and $F_{g-h}$. When all three reflections $g$, $h$ and $g-h$ are strong, there is a large chance that $F_g$ and $F_h F_{g-h}$ will have the same sign. The probability that the sign of $F_g F_h F_{g-h}$ is positive can be calculated as (Cochran, 1955)

$$P_+ = \tfrac{1}{2} + \tfrac{1}{2}\tanh(\sigma_3/\sigma_2^{3/2})E_g E_h E_{g-h} \tag{16}$$

with

$$\sigma_n = \sum_j n_j^n, \tag{17}$$

where $n_j$ are the normalized atomic scattering factors:

$$n_j = f_j \Big/ \sum_i f_i. \tag{18}$$

The application of the phase statistics to effective potentials represents an extention, valid only under the

Table 6. *Triplets determining phase relations in the (h00) row*

| $g_1$ | | | $g_2$ | | | $g_3$ | | | $U_1U_2U_3$ | $P(+)$ | Sign |
|---|---|---|---|---|---|---|---|---|---|---|---|
| 3 | 3 | 0 | 3 | −3 | 0 | 6 | 0 | 0 | 27.15 | 0.9975 | + |
| 5 | 5 | 0 | 5 | −5 | 0 | 10 | 0 | 0 | 4.79 | 0.7401 | + |
| 6 | 0 | 0 | 2 | 0 | 0 | 8 | 0 | 0 | 4.25 | 0.7200 | + |
| 6 | 0 | 0 | 4 | 0 | 0 | 10 | 0 | 0 | 2.76 | 0.6488 | + |
| 4 | 0 | 0 | 2 | 0 | 0 | 6 | 0 | 0 | 2.14 | 0.6158 | − |
| 8 | 0 | 0 | 2 | 0 | 0 | 10 | 0 | 0 | 1.61 | 0.5888 | + |
| 1 | 1 | 0 | 1 | −1 | 0 | 2 | 0 | 0 | 0.05 | 0.5026 | − |
| 5 | 3 | 0 | 5 | −3 | 0 | 10 | 0 | 0 | 2.14 | 0.6169 | + |
| 3 | 1 | 0 | 3 | −1 | 0 | 6 | 0 | 0 | 0.43 | 0.5240 | + |
| 5 | 1 | 0 | 5 | −1 | 0 | 10 | 0 | 0 | 0.032 | 0.5017 | + |

The signs in the last column are the signs of the triplets using the signs for the reflections listed in Tables 2 and 3.

restriction of atomicity which applies to the real potential, but not necessarily to the 'pseudopotential' whose Fourier coefficients are the effective structure factors. However, if the effective potentials, $U_g^{\text{eff}}$, are within the same order of magnitude as the Fourier coefficients, $U_g$, this is a reasonable assumption. The probabilities in (16) refer to (effective) normalized structure factors where the dependence on scattering angle has been removed:

$$E_g^{\text{eff}} = (1/V_c)\Big[U_g^{\text{eff}} \Big/ \sum_j f_j(s)\exp(-B_j s^2)\Big] \qquad (19)$$

with $V_c$ the unit-cell volume, $f_j$ the atomic scattering factors, $B_j$ the Debye–Waller factors, $s = \sin\theta/\lambda = g/2$ and the summation is over all atoms in the unit cell.

All triplets in the [001] projection were generated and sorted by the amplitude of the normalized effective potentials, $E_g^{\text{eff}}E_h^{\text{eff}}E_{-g-h}^{\text{eff}}$. First, triplets among ($h$00) and ($hh$0) reflections, as well as triplets determining any of these, were considered (see Table 6). The structure factors in the ($h$00) and ($hh$0) systematic rows had been determined from CBED profiles and the relative signs within each row may be assumed to be correct. The symmetry of the centrosymmetric projection [001] is $4m$ (Gjønnes *et al.*, 1995), giving equal signs for ($hk$0) and ($h\bar{k}$0). By choosing 330 positive, the origin is fixed, since $3\bar{3}0$ will then also be positive. $4n$,0,0 reflections are invariant with respect to change of origin, which leaves only the signs for $2n$,0,0 to be determined. A check of all triplets determining signs in the ($h$00) systematic row (Table 6) shows that all but two of them are consistent with the signs listed in Tables 1 and 2.

We now turn to the determination of signs for reflections outside the ($h$00) and ($hh$0) rows. The intensities of the two strongest non-systematic reflections 530 and 860 depend strongly on the relative signs involved, *i.e.* on the sign of the triplet 330, 530 and 860. Since both 530 and 860 are strong reflections appearing in several of the strongest triplets, they will influence the signs for the rest of the reflections in the projection. It was therefore decided to deduce signs for the $hk$0 reflections starting from each of the four possible combinations of signs for 530 and 860 and let the choice between them be determined by dynamical calculations at a later stage. The signs for the reflections outside the ($h$00) and ($hh$0) rows were then worked out by trial and error from the triplets by starting from the strongest triplets and continuing down the list until all the signs in the projection were determined. The stronger reflections all enter into several triplets, most of which confirmed the sign already chosen.

### 3.5. *Corrections for many-beam dynamical scattering – determination of structure factors*

We have now reached the final step in the determination of the structure factors in the [001] projection, *i.e.* the determination of structure factors from dynamical potentials. The effective potentials determined from the integrated intensities and the signs determined from triplets are now ready to be input into the Bethe expression for the dynamical potentials:

$$U_g^{\text{Bethe}} = U_g - \sum_{h\neq g}(U_h U_{g-h})/2ks_h \qquad (20)$$

with the excitation errors $2ks_h$ taken at the Bragg condition for $g$. Equation (20) is a set of coupled non-linear equations for the structure factors in terms of the dynamical (Bethe) potentials. We will attempt to solve these iteratively using the effective potentials, $U_g^{\text{eff}}$, as zeroth-order approximations to the structure factors. We rewrite (20) as

$$U_g^{(n+1)} = U_g^{\text{eff}} + \sum_{h\neq g}(U_h^{(n)}U_{g-h}^{(n)})/2ks_h \qquad (21)$$

with ($n$) the $n$th iteration and $U_g^{(0)} = U_g^{\text{eff}}$. We assume that the strong reflections are less affected by other beams and start by calculating first-order approximations to these, *i.e.* in our case with 330 the strongest and 600 the next strongest reflection:

$$U_{330}^{(1)} = U_{330}^{\text{eff}}$$

and

$$U_{600}^{(1)} = U_{600}^{\text{eff}} + U_{330}^{(1)}U_{3\bar{3}0}^{(1)}[(1/2ks_{330}) + (1/2ks_{3\bar{3}0})]$$

*etc.*, gradually introducing contributions from more beams in the calculation. The iterations were repeated until $\delta = |(U_g^n - U_g^{n-1})/U_g^n|$ was less than some preset limit; in our calculations, we used $\delta = 0.02$. Only a few iterations, 2 or 3, were needed for the strong reflections and 5–10 for the weak ones.

In the procedure described above, we assume that the intensity in reflection $g$ near its Bragg condition can be described in terms of two beams, which is a reasonable approximation for most of the reflections in the precession geometry. The two strong reflections 530 and 860, however, strongly coupled by the strong 330

reflection, enter the Bragg condition simultaneously. A three-beam case is formed, whose solution depends strongly on the relative signs involved (Fig. 7). It was therefore decided to find approximate solutions for 530 and 860, and then introduce these into the iteration scheme for the determination of the rest of the non-systematic reflections. The three diffraction conditions where 530 and/or 860 enter the Bragg condition are sketched in Fig. 7; a three-beam case formed by 330 and 860 coupled by 530, one with 530 and $3\bar{3}0$ coupled by 860 and one with 530 and 860 coupled by 330. The integrated intensity in 530 and 860 is the sum of the intensity contribution from the two relevant three-beam cases encountered in each cycle. With the assumption that the intensity can be attributed to an effective potential, this must then include an average over the two, *i.e.*

$$U_{530}^{\text{eff}} = U_{530} - U_{330}U_{860}[(1/2ks_{330}^{\text{i}}) + (1/2ks_{330}^{\text{ii}}) + (1/2ks_{860}^{\text{i}}) + (1/2ks_{860}^{\text{ii}})] \quad (22)$$

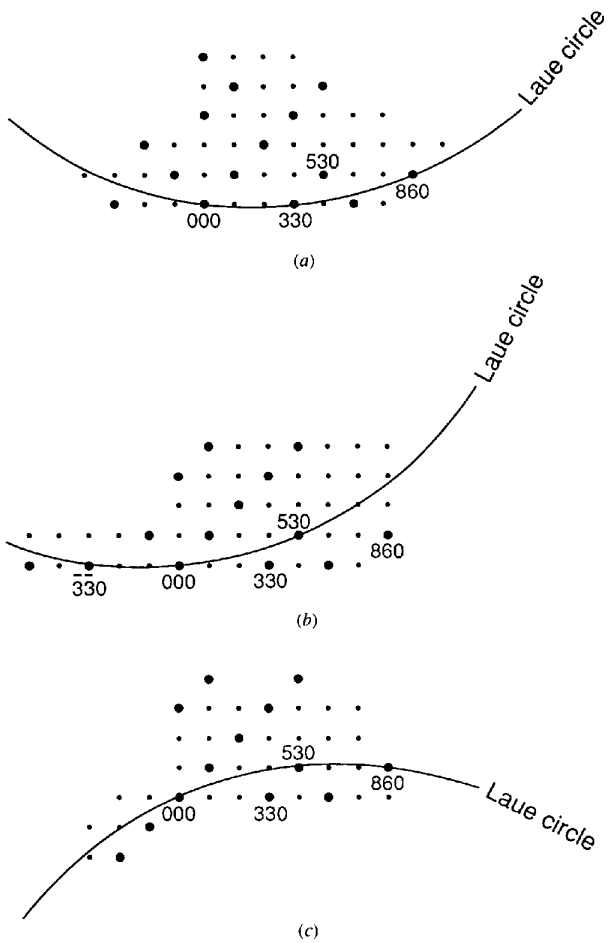


Fig. 7. The diffraction conditions with (530) and/or (860) at the Bragg condition.

Table 7. *Structure factors, $U_{530}$ and $U_{860}$, calculated from $U_{530}^{eff}$, $U_{860}^{eff}$, $U_{330}$ and the excitation errors using the Bethe formula*

| $U_{530}^{\text{eff}}$ | $U_{860}^{\text{eff}}$ | $U_{530}$ | $U_{860}$ |
|---|---|---|---|
| + | + | 0.00192 | 0.00871 |
| + | − | 0.00580 | 0.00490 |
| − | + | −0.00580 | −0.00490 |
| − | − | −0.00192 | −0.00871 |

and

$$U_{860}^{\text{eff}} = U_{860} - U_{330}U_{530}[(1/2ks_{330}^{\text{iii}}) + (1/2ks_{330}^{\text{iv}}) + (1/2ks_{530}^{\text{iii}}) + (1/2ks_{530}^{\text{iv}})], \quad (23)$$

where $s^{\text{i}}$ and $s^{\text{ii}}$ refer to excitation errors at the Bragg conditions for 530 and $s^{\text{iii}}$ and $s^{\text{iv}}$ at the Bragg condition for 860. Inserting calculated excitation errors and $U_{330}$, $U_{530}^{\text{eff}}$ and $U_{860}^{\text{eff}}$ into (21) and (22) gives the four possible combinations of $U_{530}$ and $U_{860}$ listed in Table 7, which was introduced into (21) as fixed parameters along with the ($h$00) and ($hh$0) structure factors.

The iterative solution of the Bethe equation (21) was repeated for each of the four combinations of signs for 530 and 860, this time with $U_{530}$ and $U_{860}$ as well as ($h$00) and ($hh$0) structure factors kept constant. The result is four different possible sets of structure factors, differing both in phase and in amplitude. To distinguish between these, one would have to rely either on phase statistics, especially the probability that the triplet $U_{530}U_{860}U_{330} > 0$ or a comparison between $n$-beam dynamical calculations of integrated intensities based on the structure factors and experimental intensities discussed in the next section.

### 3.6. *Dynamical n-beam calculations of precession integrated intensities in the [001] projection*

The procedures described in the previous sections have left us with four possible sets of structure factors. The choice between these was made on the basis of dynamical $n$-beam calculations. The details of the calculations will be described elsewhere (Gjønnes, 1997*b*) and only a brief outline is given here. Beams out to 1.0 Å (only ZOLZ) were included. For each reflection, the position of the Laue circle at the Bragg condition was calculated. The intensity near the Bragg condition was calculated (*i.e.* as a function of $\theta$ in Fig. 2) and integrated. At each $\theta$, the $n$ strongest beams, in terms of $U_g/2ks_g$, were included in a standard $n$-beam dynamical Bloch-wave calculation. A number of test calculations showed that 20 beams was sufficient but these change as the beam is precessed and a different selection of beams was used for each $\theta$. Test runs also showed that it was sufficent to calculate for an angular range of 0.5° near each Bragg condition.

Calculated integrated intensities for the four sets of structure factors, as well as kinematical intensities, are

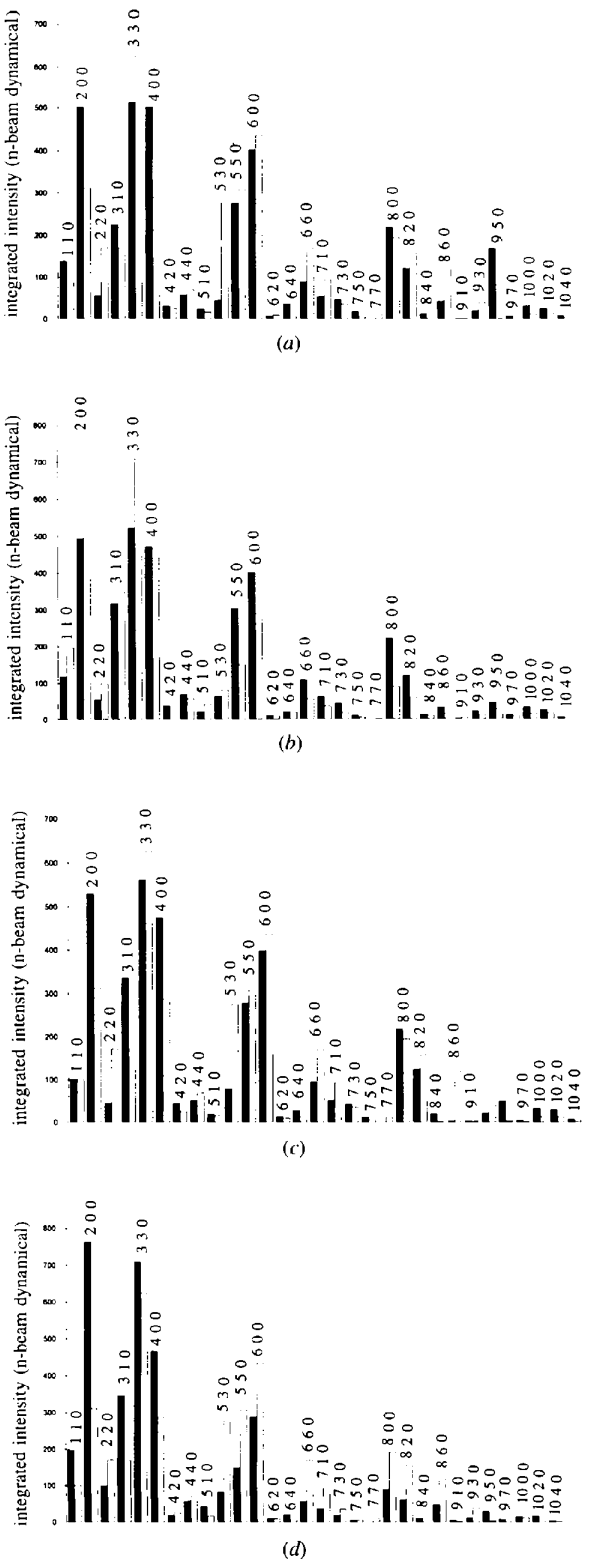


Fig. 8. Calculated (solid bars) intensities, many-beam dynamical, for four sets of structure factors: (*a*) $U_{530}^{\text{eff}} > 0$ and $U_{860}^{\text{eff}} > 0$. (*b*) $U_{530}^{\text{eff}} > 0$ and $U_{860}^{\text{eff}} < 0$. (*c*) $U_{530}^{\text{eff}} < 0$ and $U_{860}^{\text{eff}} > 0$. (*d*) $U_{530}^{\text{eff}} < 0$ and $U_{860}^{\text{eff}} < 0$ compared with experimental intensities (open bars).

reproduced in Fig. 8, for comparison with experimental intensities, as well as calculated kinematic intensities (Fig. 9) for each of the four structure-factor sets. The difference between kinematic and dynamical intensities is evident, suggesting considerable dynamical scattering. Kinematic intensities are dominated completely by the strong 330 and differences between the four different structure-factor sets are difficult to see in Fig. 9. Differences between the four sets of calculated (dynamical) integrated intensities are easily spotted (Fig. 8), especially in the relative intensities in 200 and 330. More quantitative measures of the best fit to experimental intensities are the *R* factor

$$R = \sum_g |I_g^{\text{exp}} - I_g(z)^{\text{calc}}| \Big/ \sum_g I_g^{\text{exp}} \tag{24}$$

and the correlation constant

$$\begin{aligned} \text{CC} = &\left\{ \sum_g I_g^{\text{exp}} I_g(z)^{\text{calc}} - \left( \sum_g I_g^{\text{exp}} \right) \left[ \sum_g I_g(z)^{\text{calc}} \right] \Big/ N \right\} \\ &\times \left( \left[ \sum_g (I_g^{\text{exp}})^2 - \left( \sum_g I_g^{\text{exp}} \right)^2 \Big/ N \right]^{1/2} \right. \\ &\left. \times \left\{ \sum_g [I_g(z)^{\text{calc}}]^2 - \left[ \sum_g I_g(z)^{\text{calc}} \right]^2 \Big/ N \right\}^{1/2} \right)^{-1}, \end{aligned} \tag{25}$$

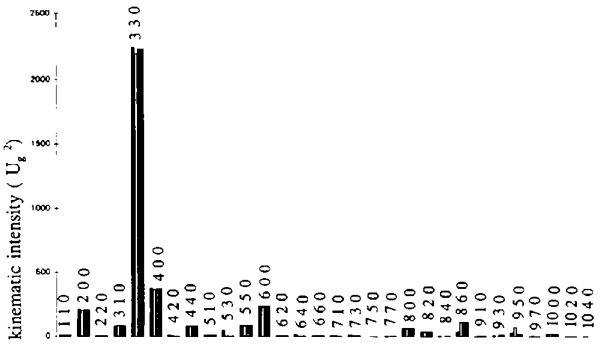


Fig. 9. Kinematical intensities calculated with: $U_{530}^{\text{eff}} > 0$ and $U_{860}^{\text{eff}} > 0$; $U_{530}^{\text{eff}} > 0$ and $U_{860}^{\text{eff}} < 0$; $U_{530}^{\text{eff}} < 0$ and $U_{860}^{\text{eff}} > 0$; $U_{530}^{\text{eff}} < 0$ and $U_{860}^{\text{eff}} < 0$.

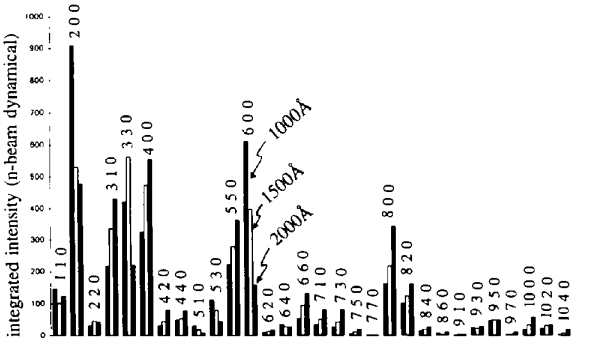


Fig. 10. Calculated integrated intensities (*n*-beam dynamical) at 1000 Å, 1500 Å and 2000 Å for $U_{530}^{\text{eff}} < 0$ and $U_{860}^{\text{eff}} > 0$.

Table 8. *R factors (R) and correlation constants (CC) between calculated intensities (n-beam dynamical) and experimental intensities for the four structure-factor sets*

| | (1) | | (2) | | (3) | | (4) | |
|---|---|---|---|---|---|---|---|---|
| | $U_{530}^{\text{eff}} > 0$ $U_{860}^{\text{eff}} > 0$ | | $U_{530}^{\text{eff}} > 0$ $U_{860}^{\text{eff}} < 0$ | | $U_{530}^{\text{eff}} < 0$ $U_{860}^{\text{eff}} > 0$ | | $U_{530}^{\text{eff}} < 0$ $U_{860}^{\text{eff}} < 0$ | |
| Thickness (Å) | $R$ | CC | $R$ | CC | $R$ | CC | $R$ | CC |
| 1000 | 0.59 | 0.74 | 0.56 | 0.76 | 0.53 | 0.76 | 0.64 | 0.68 |
| 1500 | 0.44 | 0.85 | 0.42 | 0.87 | 0.38 | 0.88 | 0.59 | 0.80 |
| 2000 | 0.62 | 0.65 | 0.67 | 0.61 | 0.65 | 0.63 | 0.51 | 0.81 |

where the the experimental and calculated intensities, $I_g^{\text{exp}}$ and $I_g(z)^{\text{calc}}$, are scaled to $\sum I_g^{\text{exp}} = \sum I_g(z)^{\text{calc}}$. $R$ factors and correlation coeffecients for the intensities were calculated for a range of thicknesses for all four structure-factor sets (Table 8). The smallest $R$ factor (38%) and the best correlation constant (88%) were found at a thickness of 1500 Å (Fig. 10) for both $U_{530}$ and $U_{860}$ negative but with $U_{860}^{\text{eff}}$ positive. $R$ factors calculated for the square root of the intensities, comparable to conventional X-ray $R$ factors, go down to 32% with a correlation constant of 93%. The structure factors are listed in Table 9.

Table 9. *Structure factors in the [001] projection*

| $h$ | $k$ | $l$ | Structure factor $U_g$ in Å$^{-2}$ |
|---|---|---|---|
| 1 | 1 | 0 | 0.00290 |
| 2 | 0 | 0 | −0.01191 |
| 2 | 2 | 0 | −0.00199 |
| 3 | 1 | 0 | 0.00662 |
| 3 | 3 | 0 | 0.03872 |
| 4 | 0 | 0 | 0.01592 |
| 4 | 2 | 0 | 0.00132 |
| 4 | 4 | 0 | 0.00750 |
| 5 | 1 | 0 | −0.00323 |
| 5 | 3 | 0 | −0.00580 |
| 5 | 5 | 0 | 0.00773 |
| 6 | 0 | 0 | 0.01275 |
| 6 | 2 | 0 | −0.00149 |
| 6 | 4 | 0 | −0.00351 |
| 6 | 6 | 0 | 0.00226 |
| 7 | 1 | 0 | 0.00209 |
| 7 | 3 | 0 | 0.00209 |
| 7 | 5 | 0 | −0.00060 |
| 7 | 7 | 0 | 0.00158 |
| 8 | 0 | 0 | −0.00653 |
| 8 | 2 | 0 | 0.00518 |
| 8 | 4 | 0 | −0.00310 |
| 8 | 6 | 0 | −0.00490 |
| 9 | 1 | 0 | −0.00188 |
| 9 | 3 | 0 | 0.00297 |
| 9 | 5 | 0 | 0.00331 |
| 9 | 7 | 0 | −0.00192 |
| 10 | 0 | 0 | 0.00356 |
| 10 | 2 | 0 | −0.00147 |
| 10 | 4 | 0 | 0.00038 |

## 4. Discussion and conclusions

In the previous sections, we have obtained ($hk0$) structure factors in Al$_m$Fe by combining data from two different experimental techniques: energy-filtered CBED profiles from the ($h00$) and ($hh0$) systematic rows and integrated intensity collected by the precession technique in the [001] projection. The *ab initio* determination of the ($h00$) and ($hh0$) structure factors was based on accurate intensity measurements and $n$-beam dynamical scattering calculations for the systematic row but non-systematics and absorption were ignored. The uncertainty in these structure factors ranges from 1% for the strongest to 20% for the weakest ones. The remaining ($hk0$) structure factors were determined from integrated intensities of much poorer accuracy, by means of two-beam-like intensity expressions; the effect of other beams was accounted for by a dynamical potential substituted for the structure factor in the two-beam expressions. The uncertainty of the remaining ($hk0$) structure factors depends on the knowledge of thickness and scaling provided by the absolute structure factors from the CBED work. An estimate is provided by the ($h00$) and ($hh0$) structure factors, which can be reproduced by the procedures decribed in §3 (when 600 is used for the scaling) to within 10–20%.

Determination of unknown structures in general requires three-dimensional intensity data, preferably a full set of integrated intensities reaching as far out in reciprocal space as possible, preferably to 1.0 Å. This can be obtained with the precession technique (Vincent & Midgley, 1994) by systematically tilting through reciprocal space (Gjønnes *et al.*, 1998). The tilted beam in the precession technique gives important advantages compared with traditional spot patterns. Very high index reflections can be excited and several Laue zones can be measured. More important, dynamical scattering is significantly reduced. However, as shown by calculations presented here, the remaining dynamical scattering may be considerable. There is thus a need to develop methods for treating integrated intensities by an approximate and workable approach in unknown structures. The present method is based on projections, since the main dynamical scattering interactions occur within the projection and because it will be important to correct the intensities for dynamical scattering prior to merging of the projections to form a three-dimensional set. Experimentally, projections will refer to different thicknesses, as well as differ widely in the $n$-beam coupling and dynamical effects. Relative intensities within systematic rows may vary from projection to projection and attempts to merge

uncorrected intensity data from several projections will invariably give inaccurate results.

A quasi-two-beam approach to dynamical scattering is used in the present treatment. Thickness and effective (dynamical) potentials $U_g^{\text{eff}}$ can be determined in two steps, provided a few structure factors in the projection have been determined by other methods, *e.g.* from CBED intensity profiles. In our example, structure factors in both the ($h$00) and the ($hh$0) rows had been determined from CBED patterns. The relative intensities in the ($h$00) row were found to be dominated by two-beam-like scattering within the systematic row and well suited as a reference in the thickness determination. The scaling of the effective structure factors was provided by 600, the strongest reflection in the ($h$00) row. The effective structure factors may in many cases represent a substantial improvement of the experimental data, especially for large thicknesses or strong reflections. At this stage in the correction procedures, we have still not made use of any phase information and the method should work equally well in non-centrosymmetric projections.

The next step, extraction of structure factors from $|U_g^{\text{eff}}|$, depends upon signs. Relative signs within the ($h$00) and ($hh$0) rows have been determined separately by CBED. The remaining signs in the centrosymmetric $Al_mFe$ [001] projection were found using statistical methods based on positive triplets. Triplets within the two systematic rows did to a large extent confirm the signs already determined from CBED patterns and it may be possible to determine all the signs in a projection from statistical methods alone, either in the simple form used here or by more advanced statistical methods. Determination of phases in the non-centrosymmetric case will certainly be more difficult and will require a more sophisticated statistical treatment of the quasi-kinematic intensities proportional to $|U_g^{\text{eff}}|^2$.

The phase determination described above has been based on a set of effective structure-factor amplitudes, which may differ in sign as well as amplitude from the

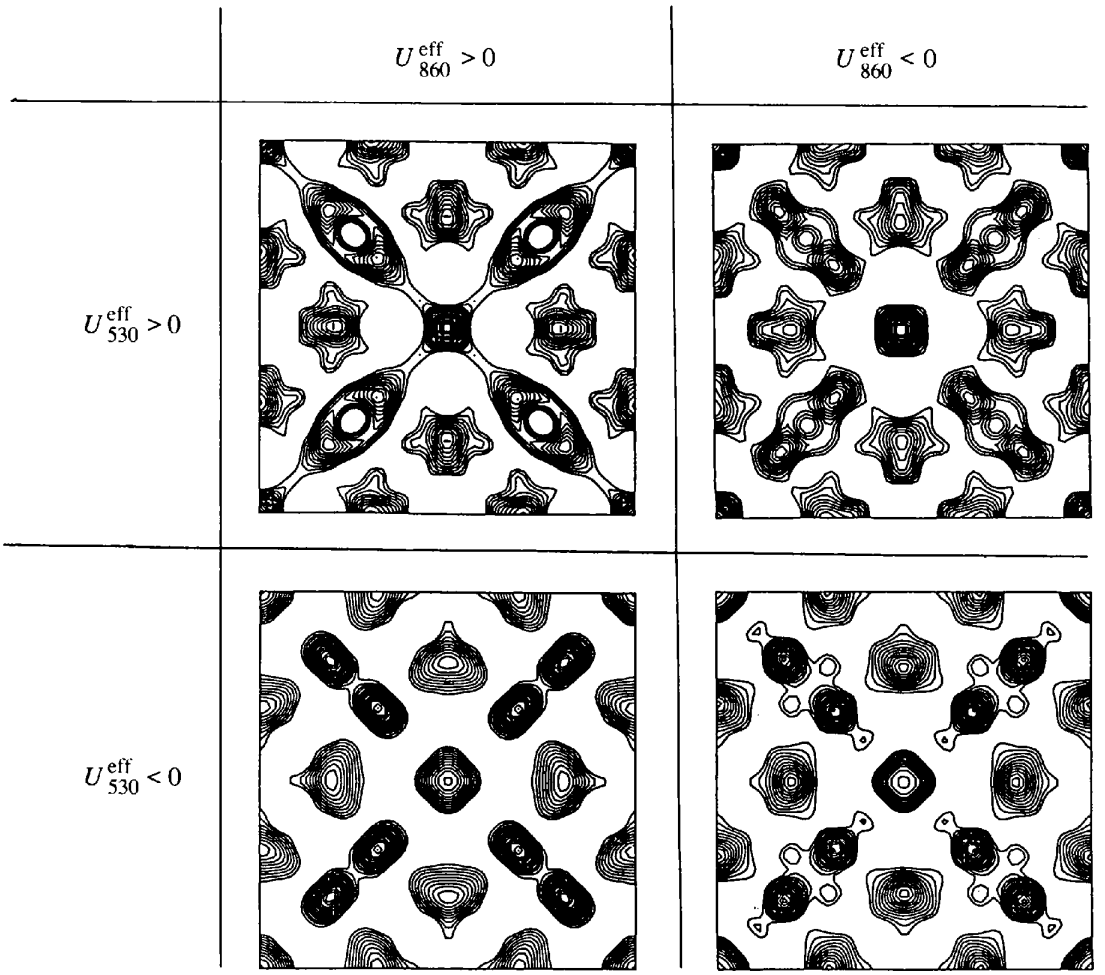


Fig. 11. Potential maps calculated with: $U_{530}^{\text{eff}} > 0$ and $U_{860}^{\text{eff}} > 0$; $U_{530}^{\text{eff}} > 0$ and $U_{860}^{\text{eff}} < 0$; $U_{530}^{\text{eff}} < 0$ and $U_{860}^{\text{eff}} > 0$; $U_{530}^{\text{eff}} < 0$ and $U_{860}^{\text{eff}} < 0$, respectively.

Table 10. *Peaks in the potential maps* $U(x, y) = \sum_{h,k} U_0 \exp[(2\pi(hx + ky)]$ *calculated from the four structure-factor sets*

| (1) $U_{530}^{\text{eff}} > 0$ $U_{860}^{\text{eff}} > 0$ | | (2) $U_{530}^{\text{eff}} > 0$ $U_{860}^{\text{eff}} < 0$ | | (3) $U_{530}^{\text{eff}} < 0$ $U_{860}^{\text{eff}} > 0$ | | (4) $U_{530}^{\text{eff}} < 0$ $U_{860}^{\text{eff}} < 0$ | |
|---|---|---|---|---|---|---|---|
| $x$ | $y$ | $x$ | $y$ | $x$ | $y$ | $x$ | $y$ |
| 0.1875 | 0.1875 | 0.1818 | 0.1818 | 0.1875 | 0.1875 | 0.1818 | 0.1818 |
| 0.3125 | 0.3125 | 0.3182 | 0.3182 | 0.3125 | 0.3125 | 0.3182 | 0.3182 |
| 0.1960 | 0.5 | 0.2040 | 0.5 | 0.1935 | 0.5 | 0.2016 | 0.5 |
| 0.3040 | 0.0 | 0.2960 | 0.0 | 0.3065 | 0.0 | 0.2984 | 0.0 |

structure factors. Still, the signs of the structure factor and effective potentials turned out to be the same for most of the reflections. In the strong 530 reflection, however, the intensity is dominated by three-beam effects including the strong 860 coupled *via* 330, resulting in opposite signs for the structure factor $U_{530}$ and the effective (or Bethe) potential $U_{530}^{\text{eff}}$. The three-beam case 530, 860 and 330 was therefore treated separately and we were left with four possible solutions, differing mainly in the signs of the two strong reflections 530 and 860, as well as minor differences in weak reflections coupled to these. To choose between the four solutions, $n$-beam dynamical calculations of $(hk0)$ integrated intensities were needed. The best fit, with an $R$ factor of 38 and 88% correlation, was obtained with $U_{530} = -0.00580$ and $U_{860} = -0.00490$ Å$^{-2}$, corresponding to an $R$ factor of 32% in structure amplitudes. This gives a combined measure of the accuracy in the intensity measurements and the two-beam approximation used in the present treatment. Unfiltered experimental intensities represent an average over thickness and diffraction conditions. Very high index reflections (further out than 1.0 Å) were not included as the measured intensities in these are more uncertain. They do, however, contribute to the dynamical scattering in the projection and this may explain why it is difficult to bring the $R$ factor below 30%.

In real space, the difference between the four different solutions is demonstrated in the potential maps reproduced in Fig. 11. The two maps for $U_{530}^{\text{eff}} > 0$ have similar features, a strong peak in the centre, strong peaks on the diagonal at approximately (0.18, 0.18) and (0.32, 0.32) as well as an irregular peak at approximately (0.5, 0.20).

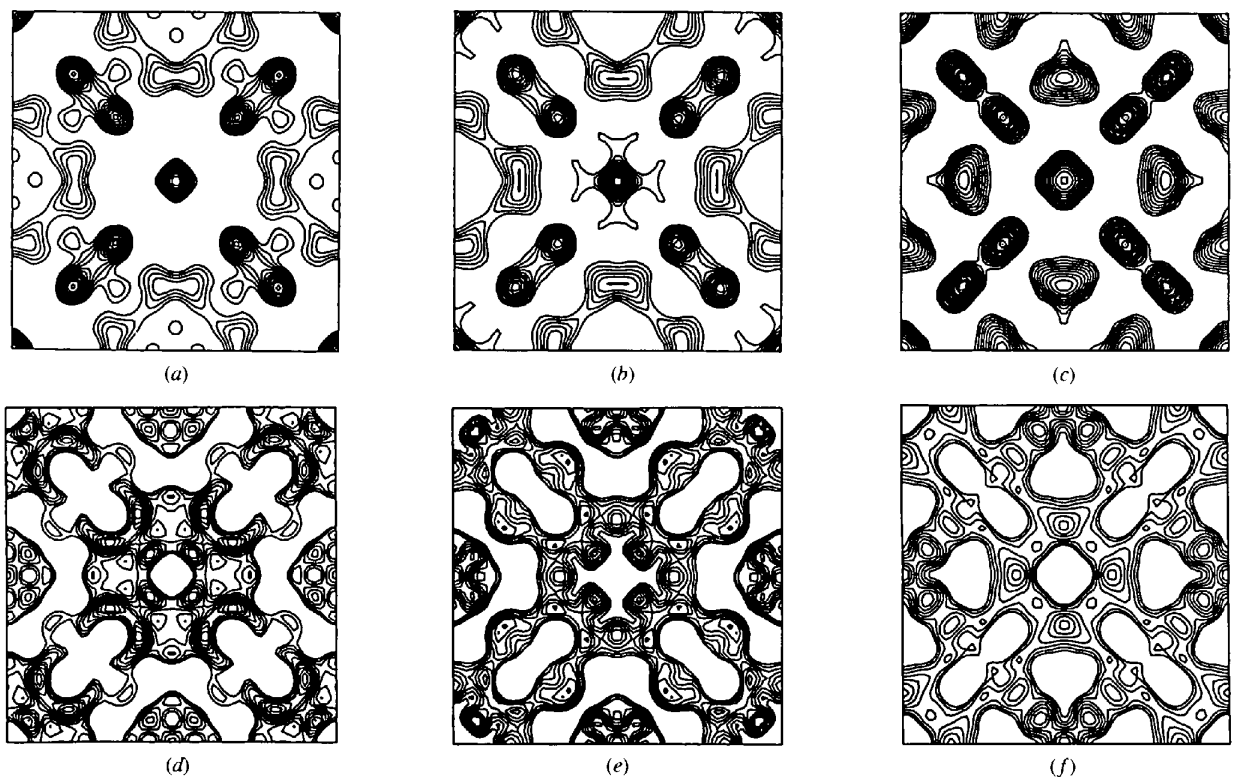


Fig. 12. Potential maps (positive and negative parts) calculated from $I_g^{1/2}$ (*a* and *d*), $U_{h00}$, $U_{hh0}$ and $I_g^{1/2}$ for the rest of the reflections (*b* and *e*), $U_g$ (*c* and *f*). Signs in (*a*), (*b*), (*d*) and (*e*) are taken from Tables 2 and 3 for *h*00 and *hh*0 reflections and from the structure model (Table 11) for the rest of the *hk*0 reflections.

The maps calculated with $U_{530}^{\text{eff}} < 0$ show quite different features, the peak at (0.5, 0.20) now has a much more regular (and reasonable) shape and the peaks on the diagonal at (0.19, 0.19) and (0.31, 0.31) are better separated (see list of peak positions in Table 10).

The effect of dynamical scattering in the precession patterns is evident and even more so in traditional spot patterns. Still, several structures have been solved from a combination of electron diffraction intensities and phase information in high-resolution images (Zou *et al.*, 1996; Weirich *et al.*, 1996; Tang, Jansen, Zandbergen & Schenk, 1995) using a kinematic approximation, though usually at smaller thicknesses. This owes more to the robustness of the various crystallographic methods employed, Patterson, Fourier and direct methods, than to the accuracy of the data in terms of $I_g \propto |U_g|^2$. A kinematic interpretation of the experimental intensities combined with chemical knowledge will in many cases give the main features of the structure, approximate atomic positions and coordination for the majority of the atoms.

One example is the parallell effort to determine the structure of $Al_mFe$ from a three-dimensional set of integrated intensities extracted from electron diffraction precession patterns (Gjønnes *et al.*, 1998). A structure model (see Table 11 for a list of preliminary $x$ and $y$ coordinates) has been derived using a variety of methods, including Patterson and Fourier syntheses as well as maximum-entropy methods, all based on the kinematical approximation. $R$ factors of 40–50% between $(I_g^{\text{exp}})^{1/2}$ and $|U_g^{\text{model}}|$ were obtained, corresponding to $R$ factors of 70% or more for the intensities, which is probably the best achievable without considering dynamical scattering for crystals as thick as these (1000 to 1500 Å). Comparison between dynamical intensities calculated

Table 11. *Preliminary x and y coordinates in $Al_mFe$ (Gjønnes et al., 1998)*

| | Atom | Occupancy | Wyckoff position | $x$ | $y$ |
|---|---|---|---|---|---|
| 1 | Fe | 1.0 | 8(*i*) | 0.180 | 0.180 |
| 2 | Fe/Al | 0.75/0.25 | 8(*i*) | 0.181 | 0.181 |
| 3 | Fe/Al | 0.75/0.25 | 8(*i*) | 0.183 | 0.183 |
| 4 | Al | 1.0 | 16(*j*) | 0.325 | 0.033 |
| 5 | Al | 1.0 | 16(*j*) | 0.319 | 0.045 |
| 6 | Al | 1.0 | 16(*j*) | 0.321 | 0.041 |
| 7 | Al | 1.0 | 4(*e*) | 0.000 | 0.000 |
| 8 | Al | 1.0 | 4(*e*) | 0.000 | 0.000 |
| 9 | Al | 1.0 | 4(*e*) | 0.000 | 0.000 |
| 10 | Al | 1.0 | 2(*b*) | 0.000 | 0.000 |
| 11 | Al | 1.0 | 8(*i*) | 0.25 | 0.25 |
| 12 | Al | 1.0 | 8(*i*) | 0.25 | 0.25 |
| 13 | Al | 1.0 | 8(*g*) | 0.5 | 0.180 |

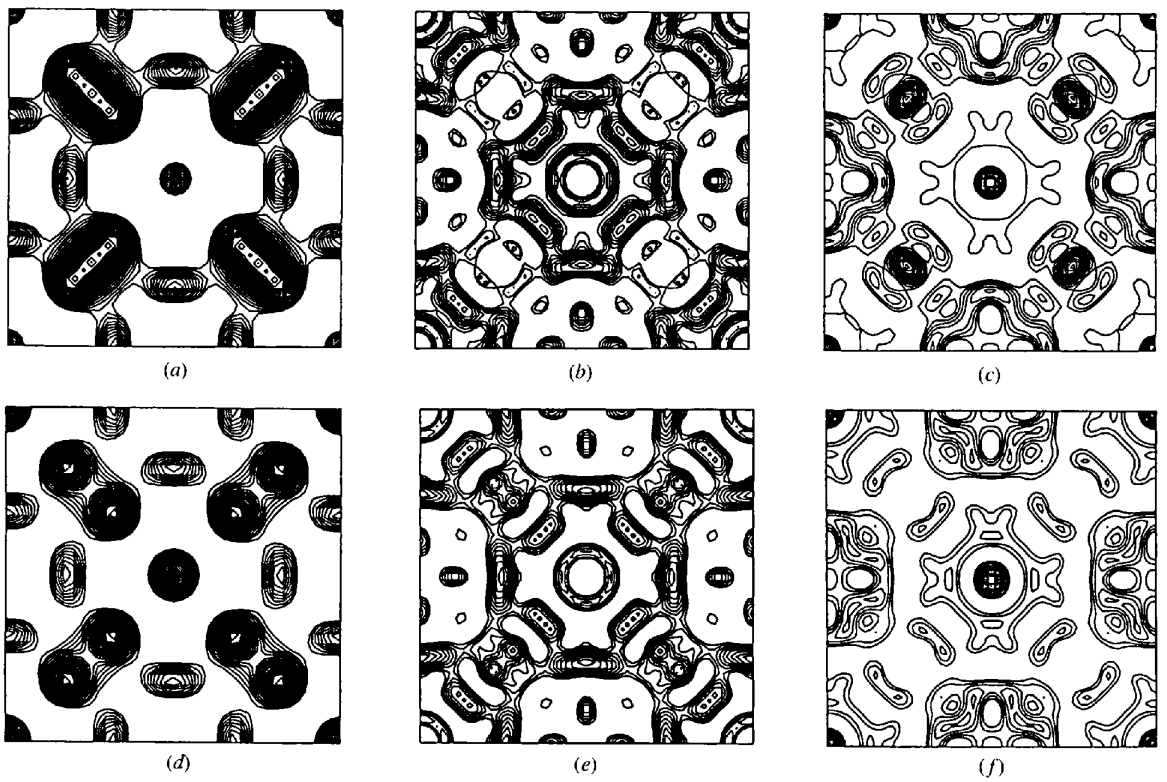


Fig. 13. Potential maps calculated from the model (Gjønnes *et al.* 1998, Table 11), with all atoms included (*a*) and only the atoms 1–10 included (*d*) and the difference map (*b* and *c* are positive and negative areas, respectively) between the $U_g$'s (this paper) and the model (*a*) and the difference map (*e* and *f*) between $U_g$'s and atoms 1–10 (*d*).

from the structure model and experimental intensities give $R$ factors as high as 80% depending on the thickness, compared with 38% for the best set of structure factors determined in this paper. The correction procedures described here thus result in a substantial improvement of the data set.

What is the significance of this in crystal structure determination? Measured intensities may be distorted by strong dynamical scattering. In a purely kinematic interpretation, this may lead to erroneous results in terms of potential maps or atomic coordinates. To better understand the effect of including dynamical scattering in the interpretation of the integrated intensities, potential maps $U_g \exp(2\pi igr)$ in the [001] projection were calculated from the structure factors, $U_g$, determined here and compared with calculations based on $I_g^{1/2}$, as well as a combination of $U_g$ for ($h$00) and ($hh$0) determined from CBED and $I_g^{1/2}$ for the rest of the reflections (Fig. 12). In the latter two, signs were taken from the CBED work (Tables 1 and 2) for the two systematic rows and from the model suggested by Gjønnes *et al.* (1998) for the rest of the reflections. The effect of removing dynamical scattering from the ($h$00) and ($hh$0) systematic rows is to remove subsidary off-diagonal peaks and emphasize the peak at (0.2, 0.5) (compare Figs. 12*a* and *b*). A further improvement is seen when all the reflections are corrected for dynamical scattering resulting in strong well separated peaks of regular shape (Fig. 12*c*), slightly shifted relative to Figs. 12(*a*) and (*b*). The enhancement of peaks as more dynamical effects are included encourages further discussion of the structure model.

Potential maps for the [001] projection were then calculated (Fig. 13*a*) for the structure model derived by Gjønnes *et al.* (1998), where most of the preliminary $x$ and $y$ coordinates (Table 11) were considered to be reasonably accurate. A few coordinates, however, are more uncertain, notably atoms 11, 12 and 13 (Table 11), which were chosen by Gjønnes *et al.* (1998) to give reasonable atomic distances and coordination but not consistently confirmed by peaks in Fourier and direct methods. To see if indications of atoms 11–13 (Table 11) could be found in the corrected ($hk$0) structure factors (this paper), a potential map was calculated using only atoms 1–10 (Fig. 13*d*). Difference maps were calculated between the corrected potential map (Fig. 12*c*) and the model including atoms 1–13 and atoms 1–10 (Figs. 13*b*,*c* and 13*e*,*f*). The strong positive peak at (0.5, 0.24) in Fig. 13(*e*) suggests that the atom at (0.5, 0.18) in the model should be moved by approximately 0.5 Å. The position of the peaks on the diagonal is slightly shifted in Fig. 11(*c*) relative to the model, in the difference Fourier a positive peak appears adjacent to a negative peak of roughly the same amplitude near the (0.18, 0.18) peak in Figs. 13(*a*) and (*d*), possibly indicating a small displacement of some of the atoms relative to the model. With only two-dimensional intensity data, we have no information on the $z$ coordinates and it is therefore not possible to know which of the atoms in the model are misplaced. While the atomic arrangement of the structure model must be considered roughly correct, some minor adjustments of $x$ and $y$ coordinates are suggested by the structure factors determined in §3 (see Table 11). This encourages a further refinement of the structure from three-dimensional intensity data along the lines suggested here. This, however, is outside the scope of this paper, but see Gjønnes *et al.* (1998) for further details on the structure determination.

The sucessful determination of unknown structures in electron diffraction will depend on many well defined intensities. Intensities extracted from spot patterns (SAD or microdiffraction) are useful at small thicknesses where they sometimes can be treated kinematically. At larger thicknesses, where dynamical effects are more serious, a combination of data from different diffraction techniques may be a better approach. In the $Al_mFe$ example presented here, absolute structure factors determined from CBED intensity profiles and integrated intensities acquired with the precession technique were combined to determine structure factors in a projection. The difficulty lies in the interpretation of the precession data, and the realization that these are dynamical intensities, though less so than in many other techniques. Still the intensities must be corrected to some degree for dynamical scattering if all the structure information is to be revealed. The approach presented here provides a first-order approximation in terms of an effective two-beam description, sufficient to bring out new structural information compared with a mere kinematical interpretation of the intensities.

Thanks are due to R. Vincent and P. A. Midgley for giving VH access to their microscope and for assistance with the precession experiment. The financial support from the Norwegian Research Council is greatly acknowledged by KG, VH and BSB. YC is grateful to the Alexander von Humboldt Foundation for an AvH fellowship.

## References

Berg, B. S. (1996). Report Series UIO/Phys/96-01. University of Oslo, Department of Physics, Oslo, Norway.
Berg, B. S., Hansen, V., Midgley, P. A. & Gjønnes, J. (1997). In preparation.
Bethe, H. (1928). *Ann. Phys. (Leipzig)*, **87**, 55–12.
Bird, D. M. & Saunders, M. (1992). *Acta Cryst.* A**48**, 555–562.
Blackman, M. (1939). *Proc. R. Soc. London Ser. A*, **173**, 68–82.
Bricogne, G. & Gilmore, C. J. (1990). *Acta Cryst.* A**46**, 284–297.
Cheng, Y. F., Nüchter, W., Mayer, J., Weickenmeier, A. & Gjønnes, J. (1996). *Acta Cryst.* A**52**, 923–936.
Cochran, W. (1955). *Acta Cryst.* **8**, 473–478.
Dorset, D. L. (1994). *Adv. Electron. Electron Phys.* **88**, 111–197.

Dorset, D. L., Kopp, S., Fryer, J. R. & Tivol, W. F. (1995). *Ultramicroscopy*, **57**, 59–89.
Gjønnes, J. (1962). *Acta Cryst.* **15**, 703–707.
Gjønnes, J., Hansen, V., Berg, B. S., Midgley, P. A. & Cheng, Y. F. (1995). *Inst. Phys. Conf. Ser.* No. 147, Section 4, pp. 121–124.
Gjønnes, J., Hansen, V., Berg, B. S., Runde, P., Cheng, Y. F., Gjønnes, K., Dorset, D. L. & Gilmore, C. (1998). *Acta Cryst.* Submitted.
Gjønnes, K. (1997*a*). *Ultramicroscopy*, **69**, 1–11
Gjønnes, K. (1997*b*). In preparation.
Gjønnes, K., Gjønnes, J., Zuo, J. M. & Spence, J. C. H. (1988). *Acta Cryst.* A**44**, 810–820.
Nüchter, W., Weickenmeier, A. & Mayer, J. (1995). Unpublished results.
Press, W. H., Flannery, B. F., Teukolsky, S. A. & Vetterling, W. T. (1988). *The Art of Scientific Computing: Numerical Recipes in Fortran*. Cambridge University Press.
Saunders, M., Bird, D. M., Midgley, P. A. & Vincent, R. (1994). Proceedings of ICEM 18, Paris, 17–22 July 1994, pp. 847–848.
Saunders, M., Bird, D. M., Zaluzec, N. J., Burgess, W., Preston, A. R. & Humphreys, C. J. (1995). *Ultramicroscopy*, **60**, 311–323.
Sayre, D. (1952). *Acta Cryst.* **5**, 60–65.
Spence, J. C. H. (1993). *Acta Cryst.* A**49**, 231–260.
Taftø, J. & Metzger, T. H. (1985). *J. Appl. Cryst.* **18**, 110–116.
Tang, D., Jansen, J., Zandbergen, H. W. & Schenk, H. (1995). *Acta Cryst.* A**51**, 188–197.
Vincent, R. & Bird, D. M. (1986). *Philos. Mag.* **53**, L35–L40.
Vincent, R., Bird, D. M. & Steeds, J. W. (1984). *Philos. Mag.* **50**, 745–763.
Vincent, R. & Midgley, P. A. (1994). *Ultramicroscopy*, **53**, 271–282.
Weirich, T. E., Ramlau, R., Simon, A., Hovmöller, S. & Zou, X. (1996). *Nature (London)*, **382**, 144–146.
Zou, X., Sundberg, M., Larine, M. & Hovmöller, S. (1996). *Ultramicroscopy*, **62**, 103–121.
Zuo, J. M. & Spence, J. C. H. (1991). *Ultramicroscopy*, **35**, 185–196.
Zuo, J. M., Spence, J. C. H. & O'Keeffe, M. (1988). *Phys. Rev. Lett.* **61**, 353–356.